**JOURNAL OF THEORETICAL AND APPLIED MECHANICS**
**63**, 1, pp. 115-129, Warsaw 2025
https://doi.org/10.15632/jtam-pl/195720

# DYNAMICS RESPONSE ANALYSIS AND MECHANICAL EXPERIMENTAL INVESTIGATION OF A DOUBLE-SPAN MULTI-SUPPORT SHAFT SYSTEM IN MICRO GAS TURBINES

Hao Lin, Leiming Song

*Beijing Jiaotong University, School of Mechanical, Electronic and Control Engineering, Beijing, China*

*corresponding author L. Song, e-mail: lmsong@bjtu.edu.cn*

Haipeng Geng, Sheng Feng

*Xi'an Jiaotong University, School of Mechanical Engineering, Xi'an, China*

Ling Li

*Beijing Jiaotong University, School of Mechanical, Electronic and Control Engineering, Beijing, China*

This study delves into analysis of dynamics and experimentation concerning a double-span multi-support shaft system in micro gas turbines. Critical speed analysis was conducted, accompanied by numerical solutions providing insights into the natural frequency. Additionally, an unbalanced response and vibration amplitude of the shaft were calculated, serving as crucial inputs for dynamic balancing considerations. The study also examined the influence of stiffness coefficient variations in bearings on the unbalance response. Dynamic balancing experiments of the motor rotor and the compressor-turbine rotor were conducted separately. Then a vibration experiment for the double-span multi-support shaft was executed at an experimental speed of 60000 r/min. The research revealed that rotors could be regarded as rigid bodies throughout the operational speed range. This study holds significant engineering implications and a practical application value.

*Keywords:* micro gas turbine, double-span multi-support shaft system, dynamics analysis, unbalance response, experiment

## 1. Introduction

### 1.1. Background

The industrialization process is increasingly constrained by resource and environmental limitations, as the high consumption and emission levels associated with industrial development are no longer sustainable. Consequently, environmental and energy concerns are gaining prominence. The utilization of reliable and stable high-end energy and power equipment emerges as a viable solution to address issues related to energy shortages and environmental pollution.

A significant portion of primary energy, approximately 66.4%, is directly dissipated into environment as thermal energy (Vishwanathan *et al.*, 2018). Notably, there exists a substantial amount of medium and low thermal energy that remains underutilized, highlighting the potential for energy recovery in micro gas turbines. Globally, the capacity of micro gas turbines ranges from 25 kW to 250 kW. Through combined generation of electricity and heat, these turbines achieve an impressive efficiency rate of 80%. Micro gas turbines offer various advantages, including a minimal number of rotating parts, compact design, small size and weight, as well as ease of assembly and maintenance (Wołowicz *et al.*, 2021; Villarroel-Schneider *et al.*, 2019). Particularly noteworthy are their low levels of pollutant emissions and noise, rendering micro gas turbines suitable for deployment in diverse facilities.

The adoption of advanced technologies, such as high-speed permanent magnet synchronous motors, flexible couplings, and elastic foil bearings, characterizes micro gas turbines. Leveraging the characteristics of high-speed and direct drive, these micro gas turbines efficiently recover energy and generate electricity (Bo *et al.*, 2018). Figure 1 illustrates the working principle of the system (Singh *et al.*, 2022).

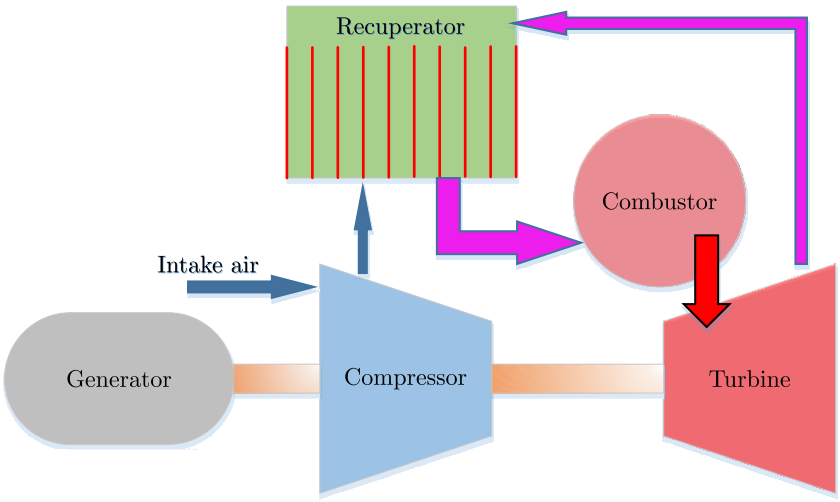


Fig. 1. The working principle of the micro gas turbine system

Ansaldo Energia (Ramaglia *et al.*, 2018) and Capstone (Othman and Boosroh, 2016) have produced micro gas turbines within the 30-200 kW power range, employing a double-span shaft with multi-supports. However, specific structural parameters and design schemes for the shaft system remain undisclosed. The pivotal technology of the high-speed shaft system, supported by oil-free lubrication bearings, significantly influences the performance of micro gas turbines, encompassing aspects like the high-speed coupling and compatibility of the bearing-shaft system. The high speed of the micro gas turbine, large pressure ratio, high efficiency, and high power density face constraints imposed by various factors. Ensuring the stable and reliable operation of the shaft system amid continuous speed improvements remains an ongoing and in-depth exploration.

The overarching objective of the industry is to maximize the operational speed of the high-speed double-span multi-support shaft system. However, achieving high rotation speed necessitates the shaft system to traverse multiple critical speeds during operation, rendering the amplitude limitation of the high-speed shaft system more challenging.

### 1.2. Research status

In the realm of high-speed, direct-drive energy machinery, the shaft system typically adopts a series structure. Power machinery with low-rated operating speeds, such as large steam turbine generators operating at 3000 r/min, commonly employs the typical series structure for the shaft system. Couplings are utilized to connect high and low-pressure rotors (permanent magnet rotors and generator rotors). The shaft system is supported by multiple bearings and encounters multiple critical speeds during operation. Under high-speed conditions, the personalized characteristics of shaft systems with varying speeds and powers render the structure of high-speed shaft systems non-universal. Notably, the amplitude limitation of the shaft system at critical speeds is particularly significant.

In the double-span shaft of the micro gas turbine, the motor rotor and turbine/compressor rotor are treated as rigid body rotors, respectively. A flexible coupling is employed to connect these two rotors. The critical speed of the flexible coupling plays a pivotal role in the overall

performance of the shaft system. Koo *et al.* (2015) conducted analysis of the vibration of a shaft supported by elastic foil bearings with a diaphragm coupling. Schmid and Pradeto (1994) studied the rotor dynamic characteristics of a high-speed motor-compressor supported by electromagnetic bearings connected via a diaphragm coupling, highlighting the diaphragm coupling role in providing a significant margin between the maximum operating speed and the critical bending frequency. Lorenzen *et al.* (1989) compared the dynamic characteristics of shaft systems connected by different couplings and found that the diaphragm coupling offered a margin between the critical speed and operating speed. The structure of the diaphragm coupling is depicted in Fig. 2.

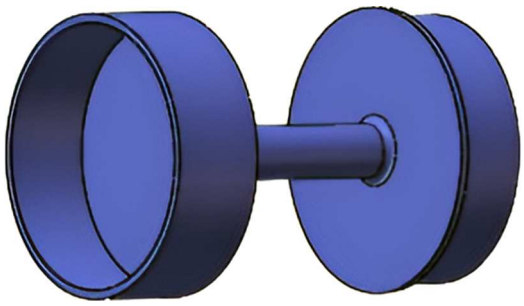

Fig. 2. Structure of the diaphragm coupling

While the aforementioned studies have delved into the dynamics of double-span multi--support shaft systems, they predominantly fall within the realm of the qualitative analysis. Emphasis has been placed on identifying reasonable critical speeds; however, there is a noticeable absence of detailed reports on the dynamic response of high-speed double-span multi-support shaft systems in micro gas turbines. Given the challenges posed by the high operating speed and the low stiffness-damping characteristics of gas bearings, successfully navigating the critical speed is a yet-to-be-resolved issue. Furthermore, insufficient attention has been devoted to elucidating strategies for traversing the first bending critical speed of the diaphragm coupling and judiciously establishing the margin between the critical speed and operational speed.

The selection of the micro gas turbine shaft system structure is multifaceted, contingent upon varying power levels and structural parameters. Following the proposal of the high-speed shaft system structure, uncertainties persist regarding the ability of elastic foil bearings to damp vibrations and the dynamic behavior of the shaft system under high-speed conditions. Beyond theoretical analysis, validation hinges on operational experiments involving the shaft system. Unfortunately, there is a paucity of related experiments for different diaphragm coupling and double-span shaft structures. Heshmat *et al.* (2014) presented an 8 kW turbine generator supported by elastic foil gas bearings connected via a diaphragm coupling. Walton *et al.* (2012) conducted operational experiments on two motors connected by a diaphragm coupling, and Heshmat and Walton (2016) experimented with a motor-flywheel supported by elastic foil gas bearings connected with a diaphragm coupling. Andrés *et al.* (2015) incorporated the diaphragm coupling in a rotor-bearing test device, yet instability was observed during the experiment at the speed range of 26000 r/min to 27000 r/min. These mixed experimental outcomes underscore the significance of experimental verification for the structure of high-speed double-span shaft systems. However, these experiments fall short of providing structure parameters and optimal dynamic characteristics for the flexible coupling, bearing, and shaft – essential for the effective operation of the shaft system. Due to the personalized structural characteristics and the scarcity of practical examples, there is a pressing need for both dynamic analysis and experimental verification of high-speed double-span shaft systems. The primary challenge lies in the complexity of the structure and the actual operation in high-speed shaft systems.

This study addresses this gap by conducting comprehensive dynamics analysis and an experiment of the double-span multi-support shaft system in a micro gas turbine. Firstly, critical speed analysis was performed in Section 2, accompanied by the provision of numerical solutions for natural frequencies. Secondly, the unbalance response and vibration amplitude of the shaft were calculated in Section 3, providing insights for dynamic balancing. The influence of stiffness coefficients of bearings on the unbalance response of the shaft system was analyzed, enabling the selection of appropriate bearing parameters for the shaft system based on the results. Thirdly, in Section 4, a balance experiment was conducted, then a vibration experiment of the double-span multi-support shaft was executed at an experimental speed of 60000 r/min, and the experimental results were employed to verify the analysis outcomes. The research methodology and results hold substantial engineering significance and a practical application value.

## 2. Analysis of critical speed and modal shape

### 2.1. Structure of the double-span multi-support shaft system

In the dynamics analysis of high-speed shaft systems, the conventional approach often involves considering two single-span rotors as rigid body modes, ensuring a sufficient margin across the operating speed range (Guan *et al.*, 2020). Adhering to these principles, the motor rotor in this study was designed with an approximately symmetrical structure, supported by two bearings. The mass distribution and moment of inertia of the motor rotor exhibit good uniformity and symmetry.

This study is grounded in practical engineering applications, specifically focusing on micro gas turbines. It provides a comprehensive understanding of the dynamics response of the shaft system, taking into account factors such as functional characteristics, power, rated speed, combination rotor structure, and load distribution of bearings (Kim *et al.*, 2023). The chosen shaft system structure is the double-span shaft, where the motor rotor is connected to the compressor-turbine rotor through a flexible coupling. Regarding support methods, there is flexibility in selecting either three or four bearings (Zywica and Baginski, 2019). The structure of the double-span multi-support shaft system for the micro gas turbine is illustrated in Fig. 3.

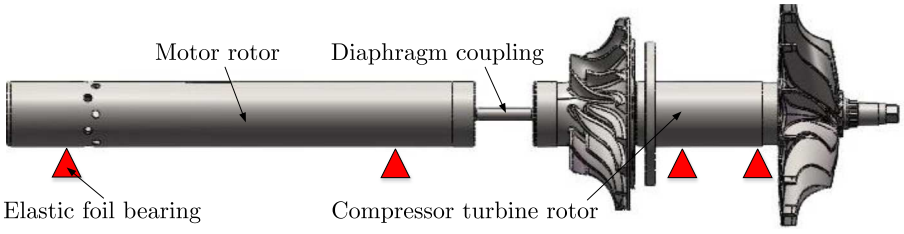


Fig. 3. Structure of the double-span multi-support shaft system

### 2.2. Theoretical model

In ensuring the stable operation of the shaft system under high-speed conditions, it is imperative to consider the vibration amplitude of the shaft, a parameter closely tied to both the natural frequency and the unbalance response of the shaft.

To delve into the vibration amplitude of the shaft system, the essential step involves determining the natural frequency. This necessitates analysis of the critical speed and modal characteristics of the shaft system (Zheng *et al.*, 2020).

Considering the diaphragms at the left and right ends of the diaphragm coupling as identical elastic components (Heshmat *et al.*, 2018), the displacement relationship between the left and right connection ends of the diaphragm coupling is illustrated in Fig. 4. In this depiction, the

shafts represent rotors at both ends and the rod of the coupling. Taking the left end as an example, node $i$ represents the node at the end of the rotor, and node $j$ represents the node at the end of the coupling rod. The lateral displacement of these two nodes is identical, whereas the angular displacement differs. The radial direction is rigid, and the lateral displacements of the nodes are expressed as $u_i$ and $v_i$.

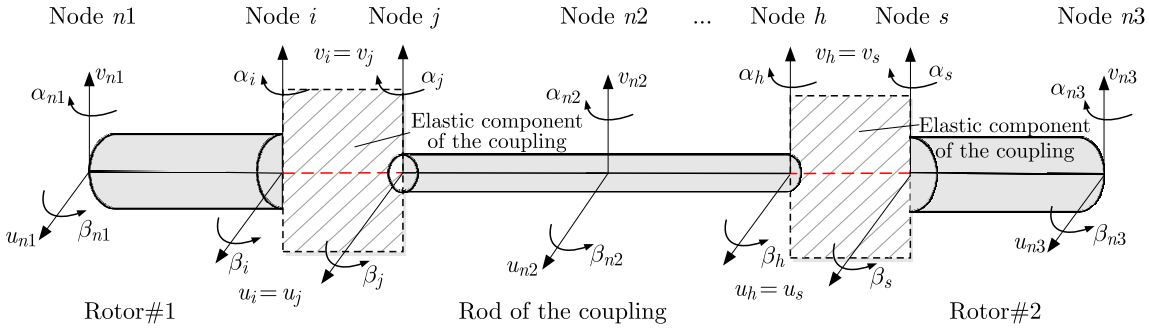


Fig. 4. Displacement relationship at the connection end of the diaphragm coupling

The column vector at the left end of the diaphragm coupling can be mathematically expressed as follows (Feng *et al.*, 2021)

$$\mathbf{q}_c = [u_{n1}, v_{n1}, \beta_{n1}, \alpha_{n1}, u_i, v_i, \beta_i, \alpha_i, \beta_j, \alpha_j, u_{n2}, v_{n2}, \beta_{n2}, \alpha_{n2}]^{\mathrm{T}} \tag{2.1}$$

The mechanical performance of the diaphragm coupling is characterized, as shown in Fig. 5.

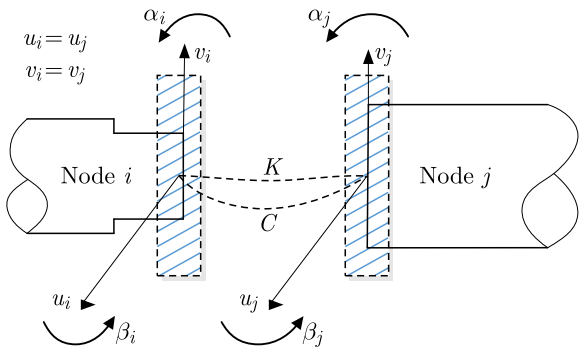


Fig. 5. Mechanical performance of the diaphragm coupling (Feng *et al.*, 2015)

The equation of motion of the shaft system was assembled by the matrix of the shaft and coupling $\mathbf{q}_c$ as follows

$$\mathbf{M}\ddot{\mathbf{q}} + \Omega\mathbf{G}\dot{\mathbf{q}} + \mathbf{K}\mathbf{q} = \mathbf{Q}(t) \tag{2.2}$$

where the mass matrix $\mathbf{M}$ includes the shaft element matrix $\mathbf{M}_e$; and the disk mass and moment of inertia matrix $\mathbf{M}_d$; the gyroscopic matrix $\mathbf{G}$ includes the gyroscopic matrix of the disk $\mathbf{G}_d$ and the gyroscopic matrix of the shaft $\mathbf{G}_e$; the stiffness matrix $\mathbf{K}$ includes the stiffness matrix of the shaft element $\mathbf{K}_e$ and the stiffness matrix of the bearing $\mathbf{K}_b$; the column vector $\mathbf{q}$ is composed of variables from each node. $\Omega$ is the rotational speed.

### 2.3. Analysis of critical speed and modal shape

In the case of a 30 kW micro gas turbine, operating in the electric motor mode, the startup phase extends from the initial stage to the self-sustaining speed or ignition speed within the range of 0-60000 r/min. Beyond the self-sustaining speed, the micro gas turbine automatically

transitions to the generator mode, where it outputs power externally, specifically at the rated operation speed of 96000 r/min. Structure parameters of the double-span multi-support shaft system are presented in Table 1.

**Table 1.** Structure parameters of the shaft system (30 kW, 96000 r/min)

| Parameter | Value |
|---|---|
| Length of shaft system [mm] | 440 |
| Length of motor rotor [mm] | 230 |
| Diameter of motor rotor [mm] | 32 |
| Length of compressor-turbine rotor [mm] | 180 |
| Diameter of compressor-turbine rotor [mm] | 32 |
| Bearing support span of motor rotor [mm] | 180 |
| Bearing support span of compressor-turbine [mm] | 40 |

To analyze the critical speed of this double-span multi-support shaft system, the calculation model, depicted in Fig. 6, was established by the finite element method. For the critical speed analysis, the right end term of Eq. (2.2) was set to zero, and the characteristic equation was solved. This process was executed using a MATLAB programme, yielding numerical solutions for the natural frequency, which are presented in Table 2.

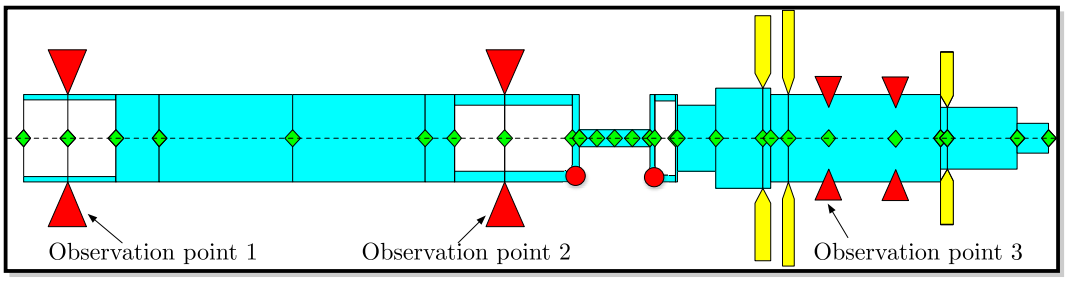


Fig. 6. Schematic diagram of the double-span multi-support shaft system model

**Table 2.** Natural frequencies of double-span multi-support shaft systems

| No. | Natural frequency [Hz] | Rotation speed [r/min] | Vibration modes |
|---|---|---|---|
| a | 319 | 19140 | Rigid body translation of compressor-turbine rotor |
| b | 337 | 20220 | Rigid body translation of compressor-turbine rotor |
| c | 392 | 23520 | Rigid body translation of motor rotor |
| d | 395 | 23700 | Rigid body translation of motor rotor |
| e | 427 | 25620 | First-order bending of diaphragm coupling |
| f | 496 | 29760 | First-order bending of diaphragm coupling |
| g | 768 | 46080 | Conical vibration of compressor-turbine rotor |
| h | 817 | 49020 | Conical vibration of compressor-turbine rotor |
| i | 1166 | 69960 | Rigid body conical vibration of motor rotor |
| j | 1217 | 73020 | Rigid body conical vibration of motor rotor |
| k | 3326 | 199560 | First-order bending of compressor-turbine rotor |
| l | 3796 | 227760 | First-order bending of compressor-turbine rotor |
| m | 3865 | 231900 | First-order bending of motor rotor |
| n | 4277 | 256620 | First-order bending of motor rotor |

The modal shapes of the shaft are illustrated in Fig. 7. The vibration modes corresponding to the rigid body are depicted in Fig. 7a to Fig. 7d and Fig. 7g to Fig. 7j. Figures 7e and 7f represent the first-order bending vibration mode of the diaphragm coupling. The first-order bending vibration modes of the motor rotor and the compressor-turbine rotor are captured in Fig. 7k to Fig. 7n. Notably, the diaphragm coupling effectively isolates bending vibrations, allowing the vibrations of the rotors to exhibit corresponding independence.

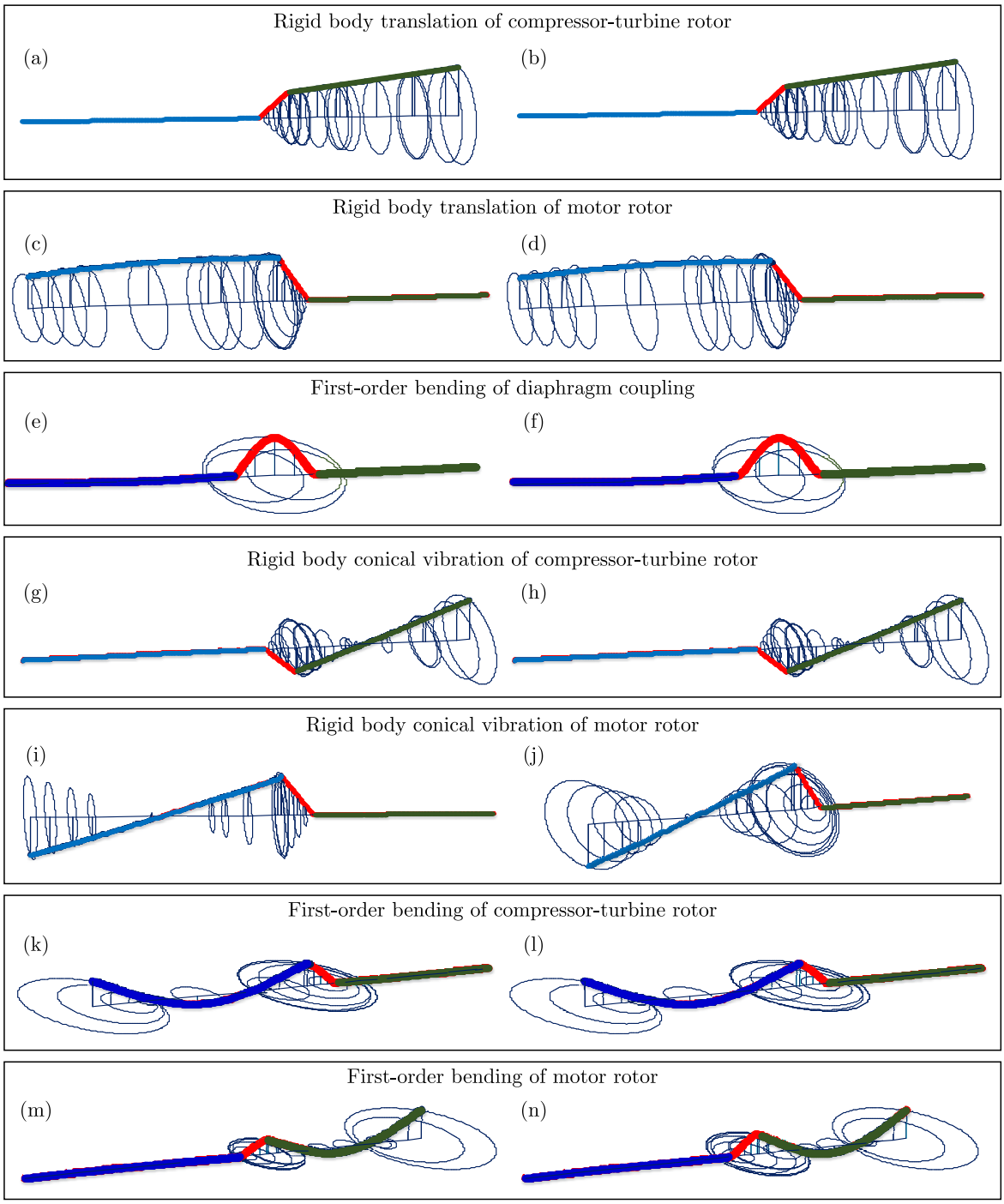


Fig. 7. Vibration mode of the double-span combined rotor shaft system

Figure 7 shows modal shapes of the double-span shaft system at the critical speed. The rigid body vibration mode of the shaft describes the rigid shape of both rotors and a flexible

deformation of the diaphragm coupling. The flexible vibration mode of the shaft is that when the rotor bends.

In the rigid vibration mode, the critical speeds of forward precession were 20220, 23700, 49020, and 73020 r/min, while the critical speeds of backward precession were 19140, 23520, 46080 and 69960 r/min. Within the rated speed range of 96000 r/min, only rigid vibration modes of the two rotors existed. The first-order bending critical speeds of the diaphragm coupling were 25620 and 29760 r/min, significantly distant from the rated speed of 96000 r/min. The first-order bending critical speeds of the rotors were 199560, 227760, 231900, and 256620 r/min, exceeding one times the rated speed. The rated speed and the bending critical speed provided ample distance, ensuring a sufficient safety margin for the dynamical performance of the shaft.

As depicted in Fig. 7, it is evident that in the low-frequency rigid body mode of the shaft, one rotor exhibits significant vibration while the other rotor experiences minimal vibration. One rotor demonstrates a rigid body vibration mode, encompassing translation and conical vibration. All modes within the rated speed range are rigid body vibrations, indicating that the operation of the shaft is unaffected by rigid body vibration modes. However, caution should be exercised to avoid bending vibration modes. The high-frequency bending modes include the first-order bending modes of the two rotors, with the bending region primarily appearing at positions of the permanent magnet and bearings.

The first-order bending critical speed of the shaft was higher than the rated speed. Rotors were regarded as rigid bodies throughout the operation speed range. The shaft had the sufficient safety margin between the rated speed and the bending critical speed.

## 3. Analysis of unbalance responses

### 3.1. Unbalance response calculation

In addition to the resonant natural frequency derived from the preceding analysis, the primary cause of vibration amplitude is the inertial centrifugal force resulting from the unbalanced mass of the rotor. This centrifugal force is directly proportional to the square of the angular speed, making the unbalance response particularly prominent in high-speed systems. The analysis of unbalance response primarily concentrates on examining the sensitivity of the rotor to unbalance at different positions. By calculating the unbalanced response, predictions regarding the vibration amplitude and frequency of the rotor during operation were made. Measures were then implemented to restrict the excessive vibration amplitude.

Given the high operating speed of the system under study, there is a stringent requirement for dynamic balance accuracy. The permissible residual unbalance is calculated as

$$U_e = 1000\frac{mG}{\omega} \tag{3.1}$$

where $U_e$ is the permissible residual unbalance [g·mm], $m$ is the rotor mass [kg], $G$ is the the numerical value of the selected balance quality grade [mm/s], $\omega$ is the angular velocity of the service speed [rad/s].

The selected balance quality grade is $G1$. The calculated maximum unbalance of the rotor is 0.263 g·mm. Leveraging the geometric and vibration characteristics of the double-span composite rotor system, unbalance values were applied at various locations, including the left end of the rotor, the center position of the permanent magnet, the thrust disk, and the center position of the disk, as depicted in Fig. 9. Observation points 1 to 3 were strategically chosen to align with the locations of three bearings in Fig. 6. Figures 8 to 11 display the amplitudes at observation points under different unbalance excitations, offering a comprehensive view of the vibration characteristics of the shaft system.

Figure 8 illustrates the response to unbalance excitation at the left end of the double-span composite rotor. Within the rated speed range of 1600 Hz, the peak frequencies of shaft vibration were approximately 506 Hz and 1222 Hz, aligning with the frequencies of rigid body vibration. These frequencies also corresponded to the natural frequencies of 496 Hz and 1217 Hz obtained in the modal analysis. This unbalance excitation mainly induced vibration at observation points 1 and 2, while observation point 3 exhibited almost no vibration response.

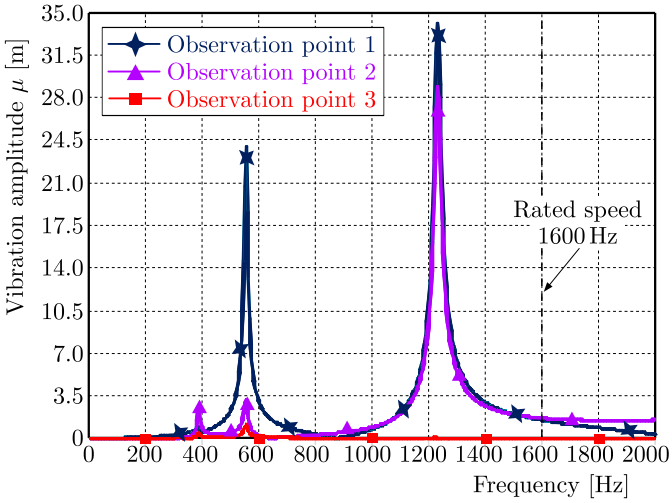


Fig. 8. Results of unbalance responses (unbalance excitation at the left end)

In Fig. 9, the unbalance excitation at the center of the permanent magnet is displayed. Within the rated speed range, the peak frequencies of rotor system vibration were approximately 400 Hz, 506 Hz, and 1222 Hz, corresponding to the natural frequencies of 395 Hz, 496 Hz, and 1217 Hz in the rotor modal analysis. Similar to Fig. 8, this unbalance excitation primarily caused vibration at observation points 1 and 2, with minimal impact on observation point 3. Comparing Fig. 8 and Fig. 9, it is evident that the unbalance excitation applied to the left end had little effect on the unbalance response at the right bearing. The amplitude of the unbalance vibration at the right bearing is considerably smaller than that at the left bearings, suggesting effective isolation by the diaphragm coupling.

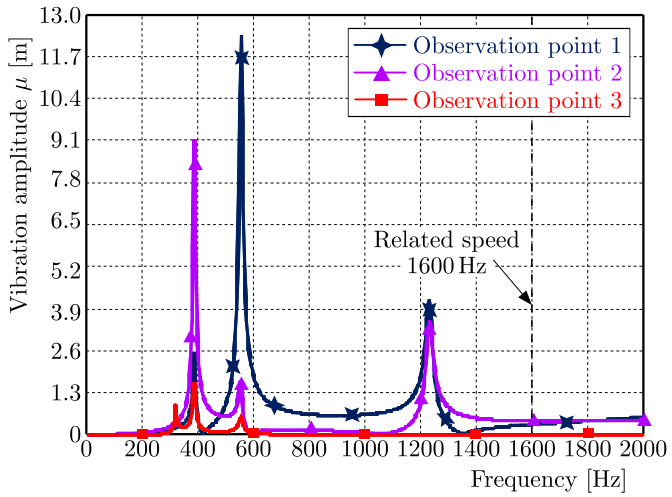


Fig. 9. Results of unbalance responses (unbalance excitation at the center of permanent magnet)

Figure 10 depicts the unbalance response to the excitation of the thrust plate. The peak vibration frequencies at observation points 1 and 2 correspond to the rigid body vibration of

the rotor. The peak frequency of vibration at observation point 3 was 300 Hz, aligning with the natural frequency of the rigid body vibration of 319 Hz obtained from modal analysis. The amplitude at observation point 3 was the highest in Fig. 10.

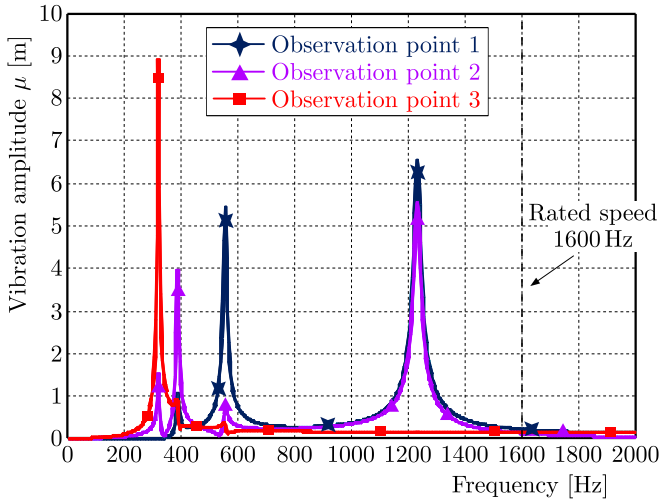


Fig. 10. Results of unbalance responses (unbalance excitation at the thrust disk)

In Fig. 11, the unbalance response to the excitation of the disk is shown, with the curve representing the response corresponding to the vibration frequency. The peak vibration frequencies at observation points 1 to 3 were consistent with those in Fig. 10. Comparing Fig. 10 and Fig. 11, it is apparent that when the unbalance was located at the right end, the vibration frequency and mode at each observation point were the same, and the amplitude at the right bearing was maximum. Thus, the vibration frequency and amplitude were related to the position of the unbalance excitation and the observation point.

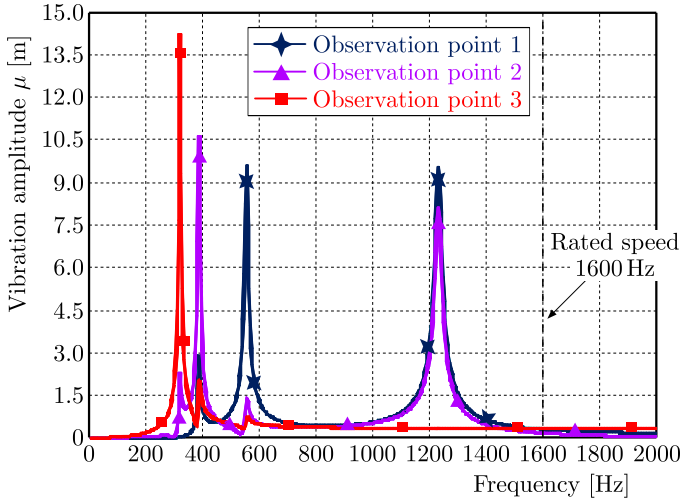


Fig. 11. Results of unbalance responses (unbalance excitation at the disk)

According to the results in Fig. 9, the unbalance response of the vibration amplitude was 35 $\mu$m at the left end of the rotor. In other cases, the maximum unbalance response did not exceed 15 $\mu$m, and most amplitudes were smaller than this value. Based on the theory of vibration analysis, the unbalance response at the same position is directly proportional to the unbalance excitation. Therefore, the unbalance response of the shaft was obtained by calculating the response at one position based on this proportional relationship.

Examining the trend of the above curves, it is apparent that within the rated speed range of 1600 Hz, the vibration amplitude near the peak frequency was larger than that at the rated speed. During the acceleration process, it is advisable to minimize prolonged stays at these frequency points.

### 3.2. Influence of bearing stiffness

In order to constrain the vibration amplitude of the shaft, various measures were implemented, including modifying the support span and adjusting the bearing stiffness. This study conducted analysis on the influence of both the bearing support span and the bearing stiffness coefficient on the system dynamics.

The bearing stiffness coefficient was varied within the range of 5e4 to 5e8 N/m, encompassing the stiffness coefficient values of various elastic foil bearings. The unbalance response of the double-span shaft was calculated under different bearing stiffness conditions, as shown in Fig. 12. The unbalance excitation was at the center of the permanent magnet. The bearing stiffness coefficients were chosen as 5e4 N/m, 5e6 N/m and 5e8 N/m.

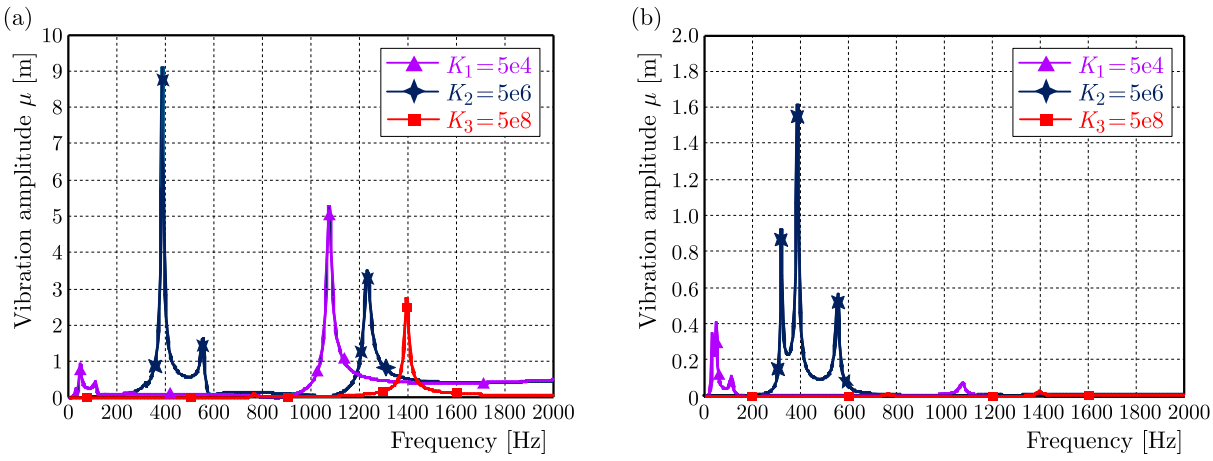


Fig. 12. Comparison of unbalance response under different bearing stiffness: (a) observation point 2, (b) observation point 3

Figure 12a depicts the unbalance response at observation point 2. The bearing stiffness had an impact on the unbalanced response. The maximum vibration amplitude approximately occured at the frequency of 400Hz, when the bearing stiffness was 5e6 N/m. The frequency range from 1000 Hz to 1600 Hz corresponded to the rigid body vibration. As the bearing stiffness increased, the vibration amplitude increased first and then decreased. In addition to the unbalance response, the selection of bearing stiffness needs to consider the stability of the shaft system.

In Fig. 12b, the unbalance response at observation point 3 is shown. At around 400 Hz, the maximum vibration amplitude corresponded to the frequency of 400 Hz with the bearing stiffness of 5e6 N/m. Comparing observation points 2 and 3, the unbalance response at observation point 3 was much smaller than that at observation point 2. Therefore, it cpuld be observed that the diaphragm coupling effectively isolated the impact of the unbalance excitation of the permanent magnet on the compressor-turbine rotor.

The insights gained from the analysis of rotor and bearing parameters hold significant importance, allowing the shaft system to select appropriate structural parameters based on the analysis results.

## 4. Mechanical experimental study of the shaft system

### 4.1. Dynamic balancing experiment

The dynamic balancing machine was depicted in Fig. 13. When the machine operates, rotation speed is measured by a photoelectric sensor. The driving power of the motor is 1.1 kW, and the maximum operation speed is 2800 r/min. The support parts are made of a non-magnetic material, which has no effect on the permanent magnet of the shaft.

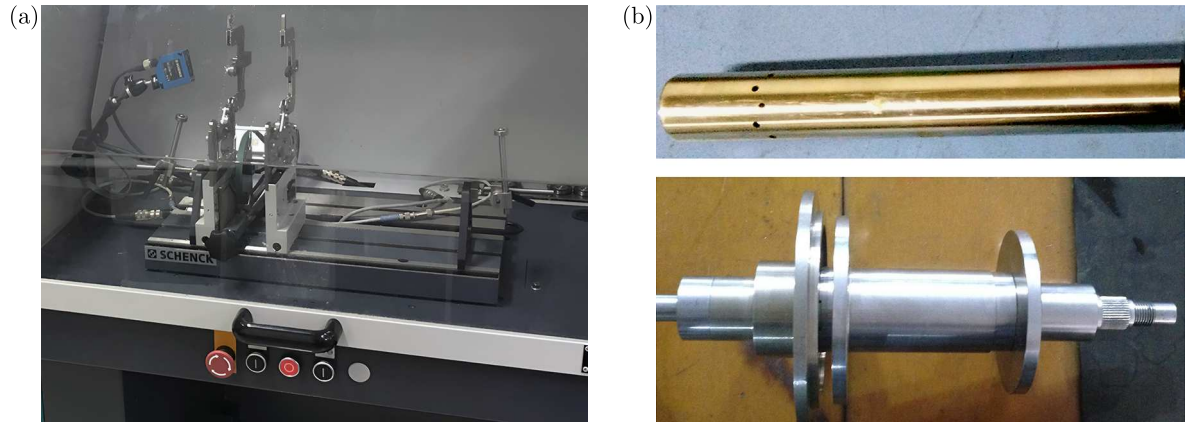


Fig. 13. Dynamic balancing experiment: (a) dynamic balancing machine, (b) motor rotor and compressor-turbine rotor

The dynamic balancing experiment of the shaft was conducted in this machine. The motor rotor and the compressor-turbine rotor were balanced separately in the rigid state because the diaphragm coupling could effectively isolate the unbalance response of the motor rotor and the compressor-turbine rotor.

According to the standard of ISO 1940 (2003), dynamic balancing results of the motor rotor and compressor-turbine rotor were obtained. Numerical values of the selected balance quality grade were $G1$.

### 4.2. High-speed dynamic experiment on the shaft system

The double-span multi-support shaft system in the micro gas turbine is illustrated in Fig. 14. The rated power of the micro gas turbine was 30 kW, and the rated speed was 96000 r/min. The shaft was propelled by a high-speed permanent magnet synchronous motor, and the operating speed was controlled within the range of 0-60000 r/min. This speed range encompassed the entire operational spectrum of the micro gas turbine, starting from 0 and reaching the self-sustaining speed or ignition speed. The experimental setup is depicted in Fig. 14.

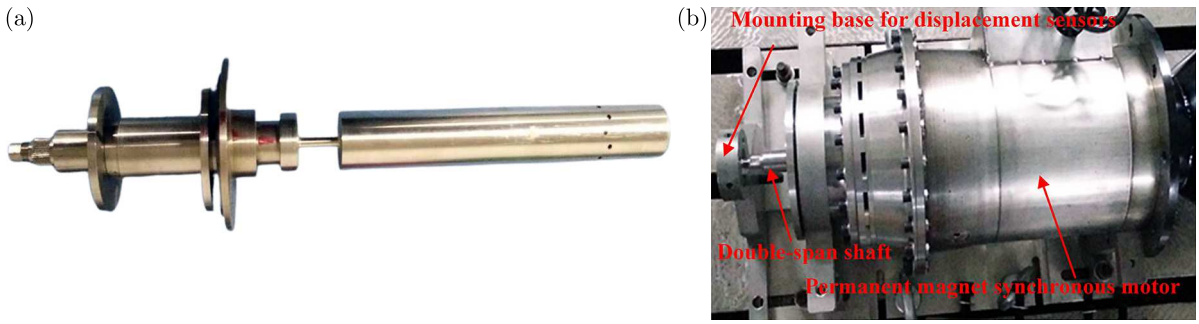


Fig. 14. Experimental device for the high-speed shaft with double spans and multiple supports: (a) double-span multi-support shaft, (b) experimental setup for the shaft

The double-span multi-support shaft was driven by the permanent magnet synchronous motor in the experimental device. The maximum experimental operating speed of the double-span multi-support shaft reached 60000 r/min. The vibration displacement of the shaft was measured by using eddy current displacement sensors.

Results of the vibration displacement for the double-span multi-support shaft at the experimental speed of 60000 r/min are presented in Fig. 15. In Fig. 15a, displacement amplitudes along the time history in vertical and horizontal directions are depicted, ranging from around 40 $\mu$m. The data of the vibration displacement was processed by the Fourier transform. Figure 15b illustrates the amplitude in the frequency domain, with the main frequency at 1000 Hz corresponding to the frequency caused by the rotor unbalance. The low-frequency at 248 Hz aligns with the rotor whirl frequency. Figure 15c shows the orbit of the shaft centerline at the speed of 60000 r/min. The experimental results validate capability of the shaft for vibration suppression and show its dynamic behavior at high speeds. The experimental findings indicate that the shaft operated effectively at the elevated speed of 60000 r/min.

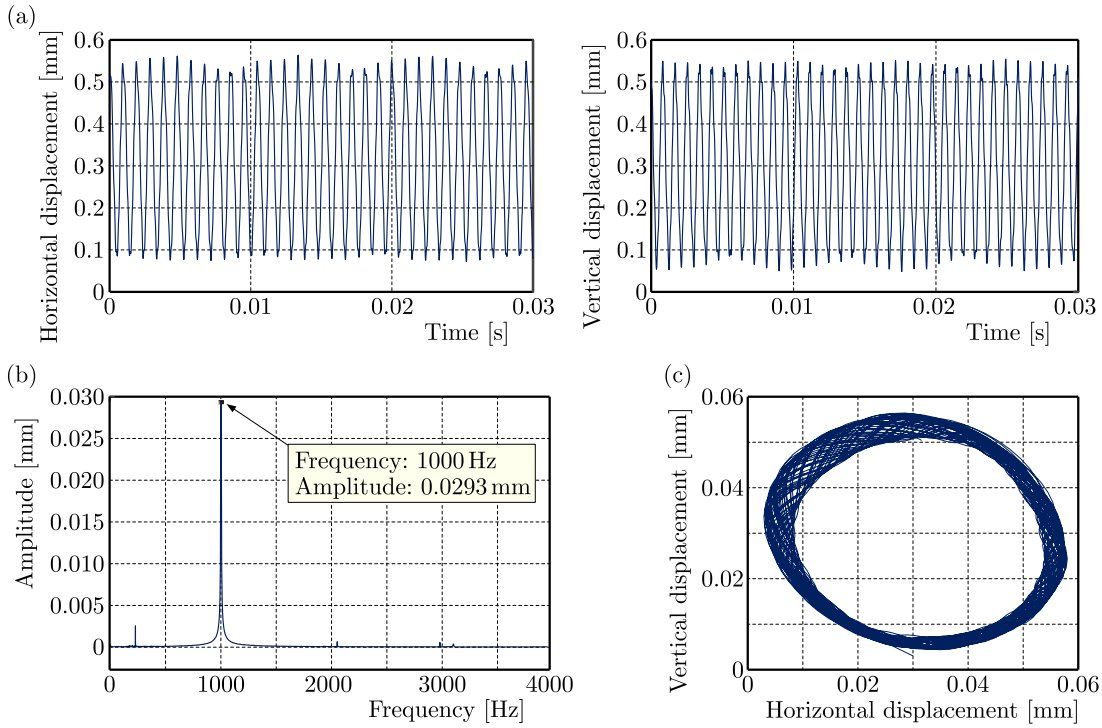


Fig. 15. Experimental vibration displacement of the shaft: (a) time domain diagram of the vibration displacement, (b) frequency of the vibration displacement, (c) shaft orbit diagram

## 5. Conclusion

This study conducted comprehensive dynamics analysis of the double-span multi-support shaft system in a micro gas turbine, leading to the following conclusions:

**Critical Speed Analysis:** The critical speed analysis was performed, providing numerical solutions for the natural frequency. The first-order bending critical speed of the shaft was found to be higher than the rated speed, with rotors considered as rigid bodies throughout the operational speed range. The shaft exhibited a sufficient safety margin between the rated speed and the bending critical speed.

**Unbalanced Response Analysis:** Unbalanced response calculations were conducted to predict vibration amplitudes of the shaft. The maximum unbalance response, located at the

left end of the rotor, was approximately 35 $\mu$m. Within the rated speed range of 1600 Hz, vibration amplitudes near peak frequencies were larger than those at the rated speed, providing valuable guidance for dynamic balance considerations.

**Effect of Bearing Stiffness:** The variation range of the bearing stiffness coefficient, selected within the range of 5e4-5e8 N/m, had an effect on the unbalance response. The unbalance response increased first and then decreased with an increase in the bearing stiffness. The analysis provided insights for selecting appropriate bearing parameters for the shaft system.

**Experimental Verification:** Experimental results at the operational speed of 60000 r/min demonstrated a vibration displacement for the double-span multi-support shaft around 40 $\mu$m. The experimental findings closely aligned with the calculated results, confirming the effectiveness of the vibration suppression and dynamic behavior of the shaft at high speeds. In future experiments, the operational speed will be increased to 96000 r/min. The nonlinear dynamic stability of the double-span multi-support shaft will be analyzed. Furthermore, considering the unbalance response and bending vibration of the flexible coupling, nonlinear dynamics of the double-span multi-support shaft will be complicated.

In summary, this study contributes valuable insights into the dynamic characteristics of the double-span multi-support shaft system, offering practical guidance for design considerations, dynamic balance, and operational performance in micro gas turbines.

*Acknowledgment*

The research was supported by the Fundamental Research Funds for the Central Universities (No. 2022JBZY028), the Beijing Natural Science Foundation (No. 3244035), Hebei Natural Science Foundation (No. E2024105047), and Science and Technology Research and Development Plan of China National Railway Group Corporation Limited (No. L2022Z002).

## References

1. Andrés L.S., Rohmer M., Park S., 2015, Failure of a test rig operating with pressurized gas bearings: a lesson on humility, *Proceedings of the ASME Turbo Expo 2015: Turbine Technical Conference and Exposition, Vol. 7A: Structures and Dynamics*, Montreal, Canada
2. Bo A., Giacomazzi E., Messina G., Di Nardo A., 2018, Analysis of a fuel flexible micro gas turbine combustor through numerical simulations, *Journal of Engineering for Gas Turbines and Power*, **140**, 12, 121504
3. Feng S., Geng H., Yu L., 2015, Rotordynamics analysis of a quill-shaft coupling-rotor-bearing system, *Proceedings of the Institution of Mechanical Engineers, Part C: Journal of Mechanical Engineering Science*, **229**, 8, 1385-1398
4. Feng S., Yang B., Tian J., Yu L., 2021, A theoretical solution of the axial stiffness of a cylindrical shell with a circular plate, *Proceedings of the Institution of Mechanical Engineers, Part C: Journal of Mechanical Engineering Science*, **235**, 18, 3563-3569
5. Guan H.Q., Feng K., Cao Y.L., Huang M., Wu Y.H., Guo Z.Y., 2020, Experimental and theoretical investigation of rotordynamic characteristics of a rigid rotor supported by an active bump-type foil bearing, *Journal of Sound and Vibration*, **466**, 115049
6. Heshmat H., Walton II J.F., 2016, Lubricant free foil bearings pave way to highly efficient and reliable flywheel energy storage system, *Proceedings of the ASME 2016 Tenth International Conference on Energy Sustainability*, 1-12
7. Heshmat H., Walton II J.F., Hunsberger A., 2014, Oil free 8 kW high-speed and high specific power turbogenerator, *Proceedings of the ASME Turbo Expo 2014: Turbine Technical Conference and Exposition, Vol. 1B: Marine; Microturbines, Turbochargers and Small Turbomachines; Steam Turbines*, Düsseldorf, Germany, 1-16

8. Heshmat H., Walton II J.F., Nicholson B.D., 2018, Ultra-high temperature compliant foil bearings: the journey to 870°C and application in gas turbine engines – experiment, *Proceedings of the ASME Turbo Expo 2018: Turbomachinery Technical Conference and Exposition, Vol. 7B: Structures and Dynamics*, Oslo, Norway
9. ISO 1940-1, 2003, Mechanical vibration-balance quality requirements for rotors in a constant (rigid) state, International Organization for Standardization
10. Kim H., Nutakor C., Singh S., Jaatinen-Värri A., Nerg J., *et al.*, 2023, Design process and simulations for the rotor system of a high-efficiency 22 kW micro-gas-turbine range extender for electric vehicles, *Mechanism and Machine Theory*, **183**, 105230
11. Koo B., Kim C.H., Lee J.S., Kim T.H., Sim K., 2015, Analysis and experimental test of a 200 kW oil-free micro gas turbine simulator, *Proceedings of the 9th IFToMM International Conference on Rotor Dynamics*, 307-319
12. Lorenzen H., Niedermann E., Wattinger W., 1989, Solid couplings with flexible intermediate shafts for high speed turbocompressor trains, *Proceedings of the Eighteenth Turbomachinery Symposium*, Texas A & M University, 101-110
13. Othman N.F., Boosroh M.H., 2016, Effect of $H_2$ and CO contents in syngas during combustion using Micro Gas Turbine, *Proceedings of IOP Conference Series: Earth and Environmental Science*, **32**, 012037
14. Ramaglia A.D., Ruedel U., Stefanis V., Florjancic S., 2018, *Ansaldo Energia Gas Turbine Technology Developments, Proceedings of the ASME Turbo Expo 2018: Turbomachinery Technical Conference and Exposition, Vol. 3: Coal, Biomass, and Alternative Fuels; Cycle Innovations; Electric Power; Industrial and Cogeneration; Organic Rankine Cycle Power Systems*, Oslo, Norway, American Society of Mechanical Engineers, New York
15. Schmied J., Pradetto J., 1994, Rotor dynamic behaviour of a high-speed oil-free motor compressor with a rigid coupling supported on four radial magnetic bearings, *Proceedings of the Second International Symposium on Magnetic Suspension Technology*, 557-573
16. Singh S., Petrov I., Pyrhönen J., Sergeant P., 2022, Conceptual design of high-speed permanent-magnet generator for a micro gas turbine, *2022 International Conference on Electrical Machines (ICEM)*, Valencia, Spain, 1696-1702
17. Villarroel-Schneider J., Malmquist A., Araoz J.A., Martí-Herrero J., Martin A., 2019, Performance analysis of a small-scale biogas-based trigeneration plant: An absorption refrigeration system integrated to an externally fired microturbine, *Energies*, **12**, 20, 3830
18. Vishwanathan G., Sculley J.P., Fischer A., Zhao J.C., 2018, Techno-economic analysis of high-efficiency natural-gas generators for residential combined heat and power, *Applied Energy*, **226**, 1064-1075
19. Walton II J.F., Heshmat H., Tomaszewski M.J., 2012, Power loss in high-speed micro turbomachinery: an experimental study, *Proceedings of the ASME Turbo Expo: Power for Land, Sea and Air*, 1-10
20. Wołowicz M., Kolasiński P., Badyda K., 2021, Modern small and microcogeneration systems-a review, *Energies*, **14**, 3, 785
21. Zheng M., Huang W., Gao C., 2020, Rotor stress and dynamics analysis of a high-speed permanent magnet machine for a micro gas turbine considering multiphysics factors, *IEEE Access*, **8**, 152523-152531
22. Żywica G., Bagiński P., 2019, Investigation of unconventional bearing systems for microturbines, *Advances in Mechanism and Machine Science, Proceedings of the 15th IFToMM World Congress on Mechanism and Machine Science*, Krakow, Poland, **73**, 1, 3439-3448

*Manuscript received February 22, 2024; accepted for publication November 8, 2024*